Structure, Ferroelectric and Dielectric Properties of $(Na_{1-2x}Ca_x)NbO_3$ Ceramics

Binzhi Liu, and Xiaoli Tan*

Department of Materials Science and Engineering, Iowa State University, Ames, Iowa 50011, USA

*Corresponding author. Email: xtan@iastate.edu

Abstract

Mimicking the scheme of incorporating La^{3+} to $Pb(Zr_{1-x}Ti_x)O_3$, Ca^{2+} is used to substitute Na^+ in the lead-free $NaNbO_3$ compound, with A-site vacancy introduced to maintain charge neutrality. The anticipated relaxor behavior is expected to suppress the remanent polarization and improve the energy storage properties of $NaNbO_3$-based ceramics. Specifically, $(Na_{1-2x}Ca_x)NbO_3$ (x = 0.01, 0.02, 0.04, 0.08) ceramics were prepared with the solid-state method and their structures and electric properties were investigated. X-ray diffraction and transmission electron microscopy reveal the existence of minor amount of $CaNb_2O_6$ second phase. Polarization *vs.* electric field hysteresis loop measurements verify the suppression of remanent polarization in compositions of $x \leq 0.04$. The temperature-dependent dielectric tests indicate that both the relaxation and diffuseness parameters monotonically increase with Ca^{2+} content. The results demonstrate that the introduction of a smaller donor dopant and charge-compensating vacancies on the A-site in $NaNbO_3$ is an effective strategy to disrupt the long-range dipole order.

Introduction

The growing demand on high-performance capacitors has revived the research on antiferroelectric ceramics as they are among the dielectrics with the highest energy-density [1, 2, 3]. In addition, antiferroelectric oxides have also shown great promise for high-strain actuators, infrared detectors, and electrocaloric cooling devices [4, 5]. These applications are based on the reversible antiferroelectric ↔ ferroelectric phase transition where the initial antiferroelectric phase is fully resumed once the applied electric field is removed, which typically manifests itself as polarization *vs.* electric field (*P*-*E*) double hysteresis loops. It is noted that the remanent polarization is close to zero in these loops.

$PbZrO_3$ is considered as the prototype compound of antiferroelectric perovskites and $PbZrO_3$-based oxide ceramics have been the most studied antiferroelectric materials [6, 7, 8, 9]. However, due to human health and environmental concerns on lead, researchers have actively searched for lead-free antiferroelectric compounds over the past few decades. Up to now, four main composition families have been explored: $(Na_{1/2}Bi_{1/2})TiO_3$-based, $BiFeO_3$-based, $AgNbO_3$-based, and $NaNbO_3$-based [10]. $(Na_{1/2}Bi_{1/2})TiO_3$-based ceramics display pinched hysteresis loops with apparent remanent polarizations at room temperature [11, 12, 13, 14]. In $BiFeO_3$-based compositions, double hysteresis loops characteristic of the antiferroelectric order have been observed [15,16,17], but the processing of these compositions has been a great challenge [18]. The processing of $AgNbO_3$-based ceramics also poses challenges and requires flowing oxygen, which results in high cost [19, 20, 21, 22].

$NaNbO_3$-based ceramics have received tremendous attention in recent years because of the ease of their processing and the readily abundant raw materials [19, 23, 24, 25, 26, 27, 28]. The base compound, $NaNbO_3$, is known for its complex structures and multiple phase

transitions: U (PE) $\xrightarrow{640\ °C}$ T_2 (PE) $\xrightarrow{575\ °C}$ T_1 (PE) $\xrightarrow{520\ °C}$ S (PE) $\xrightarrow{480\ °C}$ R (AFE) $\xrightarrow{360\ °C}$ P (AFE) $\xrightarrow{-100\ °C}$ N (FE), where PE, AFE, and FE stand for paraelectric, antiferroelectric, and ferroelectric, respectively [29]. The antiferroelectric P phase of $NaNbO_3$ at room temperature can be transformed into a ferroelectric phase, Q phase, under intense electric fields. However, the *P-E* double hysteresis loops are only reported in $NaNbO_3$ single crystals with the external field normal to the orthorhombic *c*-axis [30, 31]. In polycrystalline $NaNbO_3$ ceramics, the induced ferroelectric Q phase is metastable, and the resumption of the antiferroelectric P phase upon field removal does not occur, which leads to ferroelectric-like hysteresis loops with a large remanent polarization at room temperature. Hence, chemical modifications of $NaNbO_3$ are mainly aimed at stabilizing the antiferroelectric phase and suppressing the remanent polarization. For example, Shimizu *et al.* [24] modified $NaNbO_3$ with $CaZrO_3$ and realized double hysteresis loops with a small remanent polarization at 120 °C. The stabilized antiferroelectric phase is attributed to the reduced tolerance factor and altered average electronegativity [25].

As the reduction of remanent polarization is the major concern in $NaNbO_3$-based ceramics, relaxor ferroelectrics become relevant as they display slim hysteresis loops with minimum remanent polarization [32, 33]. It has been demonstrated that partially substituting Pb^{2+} (1.49 Å) in $Pb(Zr_{1-x}Ti_x)O_3$ with a higher-valence but smaller-size cation La^{3+} (1.36 Å) disrupts the long-range polar order and leads to a strong relaxor behavior [34, 35, 36, 37, 38]. The charge-compensating A-site vacancies, as manifested in the chemical formula $(Pb_{1-3/2x}La_x)(Zr_{1-y}Ti_y)O_3$, also contribute to the disruption of long-range polar order. Our group recently showed that the long-range dipole order in antiferroelectric perovskites can also be disrupted by introducing the relaxor behavior [39]. As a result, $(Pb_{0.97}La_{0.02})(Zr_{0.66}Sn_{0.27}Ti_{0.07})O_3$-based relaxor antiferroelectric ceramics achieved significantly reduced electric hysteresis and

ultrahigh energy efficiencies. Following the scheme of La^{3+} substituting Pb^{2+} in $(Pb_{1-3/2x}La_x)(Zr_{1-y}Ti_y)O_3$, the present research employs the addition of Ca^{2+} (1.34 Å) to substitute for Na^+ (1.39 Å) in $(Na_{1-2x}Ca_x)NbO_3$ ceramics. It is hypothesized that (1) the relaxor behavior will result, and (2) the remanent polarization can be significantly reduced. Specifically, polycrystalline ceramics of $(Na_{1-2x}Ca_x)NbO_3$ (x = 0.01, 0.02, 0.04, and 0.08) are fabricated and their structure, ferroelectric, and dielectric properties are characterized.

Results and discussion

Structure of the $(Na_{1-2x}Ca_x)NbO_3$ ceramics

In addition to the $(Na_{1-2x}Ca_x)NbO_3$ composition series, one extra composition with the nominal formula $(Na_{0.96}Ca_{0.04})NbO_{3.02}$ (denoted as NCN4$^{\#}$), is prepared for comparison. The X-ray diffraction (XRD) patterns of the $(Na_{1-2x}Ca_x)NbO_3$ ceramics (abbreviated as NCN100x) and the NCN4$^{\#}$ ceramic are shown in Fig. 1. All the ceramics have the main phase that can be indexed according to the *Pbma* orthorhombic phase of $NaNbO_3$ (PDF# 00-033-1270). The minor amount of the second phase is indexed as the columbite compound $CaNb_2O_6$ (PDF# 00-039-1392). The intensity of the $CaNb_2O_6$-phase peaks increases with increasing calcium content. The superlattice peak at around 55° of 2θ, $(21\frac{3}{4})_c$, where subscript c denotes pseudocubic notation, is characteristic of antiferroelectricity of $NaNbO_3$-based ceramics and is highlighted in Fig. 1(b). It is noted that this superlattice peak is gradually broadened and flattened in NCN100x as x increases, indicating the incorporation of Ca^{2+} to the A-site and in turn, the weakening of the antiferroelectric order in the composition series. In NCN8 (x = 0.08), the $(21\frac{3}{4})_c$ peak is about to disappear. The position of this superlattice peak slightly shifts towards higher angles, indicating that the substitution of Na^+ by Ca^{2+} decreases the size of the unit cell. This can be rationalized by

the smaller size of Ca^{2+} than Na^{+} and the creation of A-site vacancies. Furthermore, the doublet of $x = 0.01$ around 46.5° shows a merging trend into a singlet $(200)_c$, demonstrating the suppression of the oxygen-octahedra distortion by Ca doping [22].

The comparison between the NCN4 and NCN4# ceramics is quite interesting. The $(21\frac{3}{4})_c$ superlattice peak is quite strong in NCN4, but is hardly seen in NCN4#, which seems to suggest that the charge unbalance and reduction in A-site vacancy disrupt the lattice distortion and cation displacements. The extra charge provided by Ca^{2+} on the A-site in NCN4# disturbs the antiparallel dipole order and suppress the antiferroelectricity.

Figure 2 displays the scanning electron microscopy (SEM) micrographs and grain-size distributions of the composition series. The average grain size was estimated by the linear intercept method, and the bulk density was measured with the Archimedes method, both shown in Fig. 3 and listed in Table I. Ceramics of NCN1, NCN2, and NCN4 have a similar grain morphology, and the grain size decreases with the increase of calcium dopant, likely due to the presence of increased fraction of the impurity phase. Though the grain size and its distribution are very similar between NCN4 and NCN4#, the grain morphology appears to be quite different. The grains of the comparing composition, NCN4#, exhibit a strong faceting characteristic compared with its counterpart which is likely due to the excess Na. The grain size decreases from 2.31 μm to 1.70 μm with increasing calcium dopant, but the trend is reversed in NCN8. The larger grain size in NCN8 (2.71 μm) might be related to the significantly larger size of the $CaNb_2O_6$ impurity phase in this composition.

Three compositions, NCN1, NCN4, and NCN8, are selected for further transmission electron microscopy (TEM) analysis of domain structures, and the results are displayed in Fig. 4. The base compound, $NaNbO_3$, is known for the complexity of its domain structures and

superlattice diffraction spots in selected area electron diffraction (SAED) patterns. In the antiferroelectric P phase, two possible antiferroelectric domain walls are $\{100\}_c$ planes for the 90° domains and $\{110\}_c$ planes for 60° domains; in the ferroelectric Q phase, 90° domain walls habit on $\{100\}_c$ planes [40, 41]. Due to both the Nb-cation displacement and the complex oxygen octahedra tilting scheme in $NaNbO_3$-based ceramics, various types of superlattice spots are observed in SAEDs [41], including $\frac{1}{4}\{eoe\}_c$-type, $\frac{1}{2}\{eoe\}_c$-type, $\frac{1}{2}\{ooo\}_c$-type, and $\frac{1}{2}\{oeo\}_c$-type, where *e* stands for even while *o* for odd indices. The $\frac{1}{4}\{eoe\}_c$-type reflections are commonly used as the fingerprint of the existence of the antiferroelectric P phase, while the $\frac{1}{2}\{eoe\}_c$-type superlattice spot is the indicaton of the ferroelectric Q phase. According to the extensive TEM work of Guo *et al.* [41], the $\frac{1}{2}\{ooo\}_c$-type superlattice spots are a result of the oxygen octahedral tilting and can appear in both P and Q phases.

Figure 4(a) and (b) displays two representative types of NCN1 grain morphology in TEM: a hierarchical poly-domain configuration with long and thin lamellar domains arranged in micron-sized colonies [Fig. 4(a)]; and dislocation arrays associated with the second phase fine particle on the grain boundary and in the grain interior [Fig. 4(b)]. In a $[011]_c$-oriented NCN1 grain, two types of domains, ① ② ③ and ④ ⑤ ⑥ ⑦ are distinguished with the $\frac{1}{4}\{eoe\}_c$-type and the $\frac{1}{2}\{ooo\}_c$-type superlattice spots, respectively [Fig. 4(a, a_1, and a_2)]. Domains ① ② ③ are of the antiferroelectric P phase. The boundary between domain ④, ⑤, ⑥, and ⑦ are on $\{100\}_c$ planes, suggesting that they are likely 90° antiferroelectric domains. The absence of the $\frac{1}{4}\{eoe\}_c$-type superlattice spots in these domains indicates that the quadruple stacking sequence of oxygen octahedral titl and Nb-cation displacement is along either the $[010]_c$ or the $[001]_c$

directions, inclined to the zone-axis $[011]_c$. Another common feature in the NCN1 grain is that fine second phase particles are often seen with dislocations nearby [marked by bright arrows]. In the lower right part of Fig. 4(a), two dislocations penetrate the antiferroelectric domains ②, ③, and ⑦. In Fig. 4(b), a dislocation array is observed. The dislocations in NCN1 are likely formed at high temperatures due to the incompatible strain between the $CaNb_2O_6$ second phase particle and the NCN1 matrix.

TEM analysis confirms the smaller grain size of NCN4 than that of NCN1, consistent with the observation of SEM. Figure 4(c) shows the bright-field micrograph of a $[111]_c$-oriented grain in NCN4. Again, a hierarchical domain morphology with fine domains arranged in larger wedge-shape domains is seen. The corresponding SAED patterns with two sets of $\frac{1}{2}\{oeo\}_c$-type superlattice spots are recorded from domain ① and ②, shown in Fig. 4(c_1) and (c_2), respectively. The intensity of these superlattice spots is apparently weaker than those in NCN1, verifying the suppressed lattice distortions. The boundary between domain ① and ② is on the $\{01\bar{1}\}_c$ plane, suggesting domains ① and ② are of the antiferroelectric P phase. In the upper part of Fig. 4(c), three dislocations are observed [marked with dark arrows]. In Fig. 4(d), rectangular-shaped second-phase particles with facets are observed in some grains.

As the molar doping amount of calcium increases to 8%, the bulk NCN8 ceramic shows a decreased density. TEM analysis reveals two representative subgrain microstructures, as displayed in Fig. 4(e) and (f). The size of the domains decreases to hundreds of nanometers, and the boundaries between domain colonies become blurry. Two sets of thin domains orthogonal to each other are seen, with the $\frac{1}{4}\{eoe\}$-type superlattice reflections recorded. These are hence

domains of the antiferroelectric P phase. However, the contrast of these lamellar domains is significantly weaker, and the corresponding superlattice diffraction spots become much weaker as well, compared with those in NCN1. Additionally, in region ① the superlattice spots are transiting to satellite spots with long streaks, suggesting the emerging incommensurate modulation. This verifies the possibility of an incommensurate phase in $NaNbO_3$-based compositions [29], and the likely cause is the compositional heterogeneity. The existence of the $\frac{1}{4}\{eoe\}$-type superlattice spots in TEM supports the observation of the superlattice $(21\frac{3}{4})_c$ peak in XRD in NCN8. The weakened intensity of them in SAED is also consistent with the XRD results obtained from bulk samples. The second phase particles in the NCN8 ceramic are larger, but the facet feature is still preserved, as shown in Fig. 4(f).

Ferroelectric properties

Figure 5 displays the room temperature *P*-*E* loops of Ca-doped $NaNbO_3$ ceramics at a maximum electric field of 100 kV/cm at 4 Hz. The remanent polarization (P_r) and coercive field (E_c) of these ceramics (P_r is estimated as the average value of the second and the third *P*-axis intercept; E_c is taken as the average of *E*-axis intercepts) are listed in Table I. At low doping range ($x \leq 0.04$), the small values of P_r confirm that substituting Na^+ with Ca^{2+} indeed suppresses the remanent polarization. However, the NCN4$^{\#}$ and NCN8 ceramics become quite lossy at high electric fields, and the *P*-*E* hysteresis loops exhibit round tips. This might be due to the higher amount of the impurity phase of $CaNb_2O_6$. The coercive field displays a similar trend, decreasing first and reaching a minimum of 20.7 kV/cm in NCN4, and then increasing in NCN8. The increased coercive field reflects the pinning of domain walls by the increased A-site vacancies and the higher amount of the second phase particles.

Compared with that of NCN4, the *P-E* loop of NCN4$^{\#}$ becomes highly asymmetric and lossy, and the coercive field is twice that of the counterpart; and the remanent polarization is almost three times of NCN4. It seems that eliminating A-site vacancies by unbalanced charge makes the ceramic leaky. Although the lossy behavior in NCN4$^{\#}$ introduces inaccuracy in determining the remanent polarization, the comparison of the *P-E* loops between NCN4 and NCN4$^{\#}$ seems to validate that A-site vacancy facilitates the disruption of long-range dipole order and reduction of the remanent polarization.

It should be made clear that these ceramics did not seem to experience the antiferroelectric to ferroelectric phase transition during the *P-E* loop measurements at the peak field of 100 kV/cm. If higher fields are applied and the ferroelectric phase is induced, the values of P_r and E_c might be different. Attempts of applying higher peak fields result in frequent breakdown, especially in NCN4$^{\#}$ and NCN8.

Dielectric properties

The reason of incorporating Ca to $NaNbO_3$ is to impose relaxor characteristics and reduce the remanent polarization through the formation of A-site vacancies. The process can be expressed as

$$Ca^{2+} \xrightarrow{2Na^{+}} Ca_{Na}^{\cdot} + V_{Na}' \quad (1)$$

According to this reaction, the molar fraction of A-site vacancy equals to the molar fraction of Ca-dopant in NCN1, NCN2, NCN4, and NCN8. The actual concentration of A-site vacancy in these ceramics should be lower because of other parasitic reactions and the formation of the $CaNb_2O_6$ second phase. In the comparing composition NCN4$^{\#}$, A-site is fully occupied and

nominally there should be no A-site vacancies. However, the volatility of Na may have complicated the situation.

The dielectric constant and loss tangent of the Ca-doped $NaNbO_3$ ceramics under 1 MHz are plotted in Fig. 6. The main peak in the dielectric constant curves corresponds to the P-R phase transition. In NCN1 and NCN2, the major peak is quite sharp and displays an obvious first-order phase transition characteristic. In NCN1, another two minor anomalies occur at ~110 °C and ~265 °C, which are likely due to second-order phase transitions [29]. At the intermediate doping level in both NCN4 and NCN4$^{\#}$, a hump is observed at ~295 °C. While in NCN8, only the major anomaly at $T_{P\text{-}R}$ is recorded. The dielectric constant value at the main peak drops with the increase of Ca content and $T_{P\text{-}R}$ shifts towards lower temperatures. The increased defects accompanied with Ca-doping may restrain the motion of domain walls, resulting in decreased dielectric constant.

Furthermore, the main dielectric peak gets broadened as Ca-dopant increases, suggesting a trend towards enhanced relaxor behavior. The relaxor characteristics can be quantitively analyzed by fitting the equation [42,43]

$$\frac{\varepsilon_{m,r}}{\varepsilon_r} = 1 + \frac{(T-T_m)^{\gamma}}{2\delta^2} \quad (2)$$

The parameter γ indicates the degree of dielectric relaxation and δ (this symbol is not the phase angle in loss tangent tan δ) represents the diffuseness of the phase transition at T_m, which is the P-R phase transition temperature $T_{P\text{-}R}$ at the major dielectric peak in NCN ceramics. Equation (2) regresses to the Curie-Weiss law at $\gamma = 1$, which represents a typical first-order phase transition; Eq. (2) denotes a prototypical relaxor behavior at $\gamma = 2$. When γ and δ increases, relaxor characteristic is enhanced. For the studied compositions, γ and δ are calculated from fitting the 1 MHz data in the temperature range from $T_{P\text{-}R}$ + 40 °C to $T_{P\text{-}R}$ + 150 °C. Their values are plotted

in Fig. 7 and listed in Table 1. It is evident both parameters increase with x in $(Na_{1-2x}Ca_x)NbO_3$ ceramics. Compared with the composition NCN4, NCN4$^{\#}$ has smaller relaxation and diffuseness parameters, suggesting that A-site vacancies promote relaxor behavior.

Given the complex nature in crystal structures and phase transition sequence in $NaNbO_3$-based ceramics, it is still challenging at this stage to have a precise picture of the impact of Ca-dopant. The formation of A-site vacancies and the second phase accompanied with Ca-doping exacerbates the situation. However, combining all the experimental data presented here, it seems to be evident that Ca-dopant reduces the lattice distortion, weakens the antiferroelectric structure feature, disrupts the long-range dipole order, and introduces relaxor characteristics. The trend is in the right direction toward the initial objective of realizing a relaxor antiferroelectric ceramic. Even though regular double hysteresis loops with a minimum remanent polarization are not achieved in $(Na_{1-2x}Ca_x)NbO_3$ ceramics, the idea of substituting Na^+ with smaller size and higher valance cations should still be pursued in other systems.

Conclusions

Aiming to reduce the remanent polarization through introducing relaxor characteristics, ceramics of $(Na_{1-2x}Ca_x)NbO_3$ (x = 0.01, 0.02, 0.04, and 0.08) are prepared and their structure and properties are characterized. XRD indicates that substitution of Na^+ in $NaNbO_3$ with Ca^{2+} reduces the lattice distortion and weakens the antiferroelectric structure feature. Correspondingly, TEM reveals a gradually decreasing density of antiferroelectric domains with streaking superlattice diffraction spots as Ca-dopant increases. Under the peak field of 100 kV/cm, the antiferroelectric to ferroelectric phase transition was not triggered; but the *P*-*E* measurement verifies the suppression of the remanent polarization in compositions of $x \leq 0.04$.

The relaxation and diffuseness parameters increase with Ca-content in $(Na_{1-2x}Ca_x)NbO_3$ ceramics, confirming the enhancing trend of the relaxor characteristics. The comparison between ceramics of $(Na_{0.92}Ca_{0.04})NbO_3$ and $(Na_{0.96}Ca_{0.04})NbO_{3.02}$ verifies the important role A-site vacancy plays in introducing the relaxor behavior.

Methodology

Ceramics of $(Na_{1-2x}Ca_x)NbO_3$, denoted as NCN100x, were synthesized using the solid-state reaction method. One additional composition $(Na_{0.96}Ca_{0.04})NbO_{3.02}$, abbreviated as NCN4$^{\#}$, was also prepared to compare with NCN4. Raw powders of high purity (≥ 99.9%) of $NaCO_3$, $CaCO_3$, and Nb_2O_5 were first baked for 48 hours at 250 °C to remove moisture. The baked powders were batched in quantities according to the chemical formula and mixed in a vibratory mill for 10 hours with zirconia media in 100% ethanol. After drying for 24 hours, the powder was calcined at 800 °C for 4 hours. The calcined powder was re-milled for another 10 hours and dried for 24 hours. Then, the powder was mixed with a 10 wt.% polyvinyl alcohol binder and uniaxially pressed into pellets at a pressure of 150 MPa; the size of the green compact was 11 mm in diameter and ~2 mm in thickness. The pellets were de-bindered at 600 °C for 3 hours and then sintered at different temperatures ranging from 1330 °C to 1380 °C for 2 hours, depending on the composition. A heating rate of 2 °C/min was used during sintering while the compact was buried in the protective powder of the same composition.

The crystal structure and phase purity of the sintered ceramics were examined with X-ray diffraction (XRD) using Cu-Kα radiation in the 2θ range of ~20° – 60° on a Rigaku SmartLab diffractometer operated at a voltage of 40 kV and a current of 44 mA. The bulk density of the samples was measured using the Archimedes method. The surface of the as-sintered ceramic

samples was examined with scanning electron microscopy (SEM, FEI Inspect 50) to reveal the grain size and morphology. The domain structure within the grains was characterized using transmission electron microscopy (TEM) on an FEI Tecnai G2-F20 (S)TEM. The TEM specimen preparation followed the standard procedure involving ultrasonic cutting, dimpling, polishing, annealing, and Ar-ion milling.

For the measurement of the polarization response under the applied field, samples were first ground to a thickness of ~0.2 mm, and silver electrodes of 2 mm diameter were sputtered on both sides of the samples. The *P*-*E* hysteresis loops were measured at room temperature at the peak field of 100 kV/cm and a frequency of 4 Hz, using a standardized ferroelectric test system (Precision LC II, Radiant Technologies). For the dielectric constant measurement, silver paste was fired on both sides of the ceramics at 800 °C for 10 min as electrodes. The measurements were performed during heating at the rate of 4 °C/minute at the frequency of 1 MHz with an LCR meter (HP-4284A, Hewlett-Packard).

Acknowledgments

This work was supported by the USA National Science Foundation (NSF) through Grant No. DMR-1700014. The authors are grateful for Prof. David Cann's suggestion of the material system and critical reading of the manuscript.

Table I: Summary of the structure and properties of the Ca-doped $NaNbO_3$ ceramics.

Composition	Grain size (μm)	Density (g/cm^3)	T_{P-R} (°C)	γ	δ	P_r ($\mu C/cm^2$)	E_c (kV/cm)
NCN1	2.31	4.13	355.9	1.14	14.39	0.96	25.81
NCN2	1.84	4.15	349.9	1.20	18.01	0.62	21.19
NCN4	1.72	4.15	337.7	1.25	20.41	0.65	20.72
NCN4$^{\#}$	1.70	4.14	336.2	1.20	19.71	2.16	41.48
NCN8	2.71	4.12	231.3	1.32	32.08	1.86	56.76

References

1. **S. Kwon, W. Hackenberger, E. Alberta, E. Furman, and M. Lanagan:** Nonlinear dielectric ceramics and their applications to capacitors and tunable dielectrics. *IEEE Electr. Insul. Mag.* **27**, 43 (2011).
2. **A. Chauhan, S. Patel, R. Vaish, and C.R. Bowen:** Anti-ferroelectric ceramics for high energy density capacitors. *Materials* **8**, 8009 (2015).
3. **L. Yang, X. Kong, F. Li, H. Hao, Z. Cheng, H. Liu, J-F. Li, and S. Zhang:** Perovskite lead-free dielectrics for energy storage applications. *Prog. Mater. Sci.* **102**, 72 (2019).
4. **W.Y. Pan, C.Q. Dam, Q.M. Zhang, and L.E. Cross:** Large displacement transducers based on electric field forced phase transitions in the tetragonal $(Pb_{0.97}La_{0.02})(Ti,Zr,Sn)O_3$ family of ceramics. *J. Appl. Phys.* **66**, 6014 (1989).
5. **B. Lu, P. Li, Z. Tang, Y. Yao, X. Gao, W. Kleemann, and S-G. Lu:** Large electrocaloric effect in relaxor ferroelectric and antiferroelectric lanthanum doped lead zirconate titanate ceramics. *Sci. Rep.* **7**, 45335 (2017).
6. **Q. Tan, Z. Xu, and D. Viehland:** Effect of substituents with different valences on antiferroelectric stability of antiferroelectric lead zirconate ceramics. *J. Mater. Res.* **14**, 4251 (1999).
7. **R.E. Koritala, M.T. Lanagan, N. Chen, G.R. Bai, Y. Huang, and S.K. Streiffer:** Microstructure and properties of $PbZr_{0.6}Ti_{0.4}O_3$ and $PbZrO_3$ thin films deposited on template layers. *J. Mater. Res.* **15**, 1962 (2000).
8. **A.K. Tagantsev, K. Vaideeswaran, S.B. Vakhrushev, A.V. Filimonov, R.G. Burkovsky, A. Shaganov, D. Andronikova, A.I. Rudskoy, A.Q.R. Baron, H. Uchiyama, D. Chernyshov, A. Bosak, Z. Ujma, K. Roleder, A. Majchrowski, J-H. Ko, and N. Setter:** The origin of antiferroelectricity in $PbZrO_3$. *Nat. Commun.* **4**, 2229 (2013).
9. **X. Hao, J. Zhai, L.B. Kong, and Z. Xu:** A comprehensive review on the progress of lead zirconate-based antiferroelectric materials. *Prog. Mater. Sci.* **63**, 1 (2014).
10. **X. Tan, C. Ma, J. Frederick, S. Beckman, and K.G. Webber:** The antiferroelectric ↔ ferroelectric phase transition in lead-containing and lead-free perovskite ceramics. *J. Am. Ceram. Soc.* **94**, 4091 (2011).
11. **S-T. Zhang, A.B. Kounga, W. Jo, C. Jamin, K. Seifert, T. Granzow, J. Rödel, D. Damjanovic:** High-strain lead-free antiferroelectric electrostrictors. *Adv. Mater.* **21**, 4716 (2009).
12. **W. Jo, R. Dittmer, M. Acosta, J. Zang, C. Groh, E. Sapper, K. Wang, and J. Rödel:** Giant electric-field-induced strains in lead-free ceramics for actuator applications–status and perspective. *J. Electrocerams*. **29**, 71 (2012).
13. **E-M. Anton, L.A. Schmitt, M. Hinterstein, J. Trodahl, B. Kowalski, W. Jo, H-J. Kleebe, J. Rödel, and J.L. Jones:** Structure and temperature-dependent phase transitions of lead-free $Bi_{1/2}Na_{1/2}TiO_3$-$Bi_{1/2}K_{1/2}TiO_3$-$K_{0.5}Na_{0.5}NbO_3$ piezoceramics. *J. Mater. Res.* **27**, 2466 (2012).
14. **J. Ding, Y. Liu, Y. Lu, H. Qian, H. Gao, H. Chen, and C. Ma:** Enhanced energy-storage properties of $0.89Bi_{0.5}Na_{0.5}TiO_3$–$0.06BaTiO_3$–$0.05K_{0.5}Na_{0.5}NbO_3$ lead-free anti-ferroelectric ceramics by two-step sintering method. *Mater. Lett.* **114**, 107 (2014).

15. D. Chen, C.T. Nelson, X. Zhu, C.R. Serrao, J.D. Clarkson, Z. Wang, Y. Gao, S-L. Hsu, L.R. Dedon, Z. Chen, D. Yi, H-J. Liu, D. Zeng, Y-H. Chu, J. Liu, D.G. Schlom, and R. Ramesh: A strain-driven antiferroelectric-to-ferroelectric phase transition in La-doped $BiFeO_3$ thin films on Si. *Nano Lett.* **17**, 5823 (2017).

16. S. Karimi, I.M. Reaney, I. Levin, and I. Sterianou: Nd-doped $BiFeO_3$ ceramics with antipolar order. *Appl. Phys. Lett.* **94**, 112903 (2009).

17. T. Rojac, A. Bencan, G. Drazic, M. Kosec, and D. Damjanovic: Piezoelectric nonlinearity and frequency dispersion of the direct piezoelectric response of $BiFeO_3$ ceramics. *J. Appl. Phys.* **112**, 064114 (2012).

18. T. Rojac, A. Bencan, B. Malic, G. Tutuncu, J.L. Jones, J.E. Daniels, and D. Damjanovic: $BiFeO_3$ ceramics: processing, electrical, and electromechanical properties. *J. Am. Ceram. Soc.* **97**, 1993 (2014).

19. A. Kania and J. Kwapulinski: $Ag_{1-x}Na_xNbO_3$ (ANN) solid solutions: from disordered antiferroelectric $AgNbO_3$ to normal antiferroelectric $NaNbO_3$. *J. Phys. Condens. Matter*. **11**, 8933 (1999).

20. L. Zhao, Q. Liu, S. Zhang, and J-F. Li: Lead-free $AgNbO_3$ anti-ferroelectric ceramics with an enhanced energy storage performance using MnO_2 modification. *J. Mater. Chem. C* **4**, 8380 (2016).

21. Y. Tian, L. Jin, H. Zhang, Z. Xu, X. Wei, E.D. Politova, S.Y. Stefanovich, N.V. Tarakina, I. Abrahams, and H. Yan: High energy density in silver niobate ceramics. *J. Mater. Chem. A* **4**, 17279 (2016).

22. J. Gao, Y. Zhang, L. Zhao, K-Y. Lee, Q. Liu, A. Studer, M. Hinterstein, S. Zhang, and J-F. Li: Enhanced antiferroelectric phase stability in La-doped $AgNbO_3$: perspectives from the microstructure to energy storage properties. *J. Mater. Chem. A* **7**, 2225 (2019).

23. Y. Xu, W. Hong, Y. Feng, and X. Tan: Antiferroelectricity induced by electric field in $NaNbO_3$-based lead-free ceramics. *Appl. Phys. Lett.* **104**, 052903 (2014).

24. H. Shimizu, H. Guo, S.E. Reyes-Lillo, Y. Mizuno, K.M. Rabe, and C.A. Randall: Lead-free antiferroelectric: $xCaZrO_3$-$(1-x)NaNbO_3$ system ($0 \leq x \leq 0.10$). *Dalton Trans.* **44**, 10763 (2015).

25. H. Guo, H. Shimizu, Y. Mizuno, and C.A. Randall: Strategy for stabilization of the antiferroelectric phase (*Pbma*) over the metastable ferroelectric phase (*$P2_1ma$*) to establish double loop hysteresis in lead-free $(1-x)NaNbO_3$-$xSrZrO_3$ solid solution. *J. Appl. Phys.* **117**, 214103 (2015).

26. H. Qi, R. Zuo, A. Xie, A. Tian, J. Fu, Y. Zhang, and S. Zhang: Ultrahigh energy-storage density in $NaNbO_3$-based lead-free relaxor antiferroelectric ceramics with nanoscale domains. *Adv. Funct. Mater*. **29**, 1903877 (2019).

27. S. Prasertpalichat and D.P. Cann: Crystal structure and electrical properties of complex perovskite solid solutions based on $(1-x)NaNbO_3$-$xBi(Zn_{0.5}Ti_{0.5})O_3$. *J. Electroceram.* **33**, 214 (2014).

28. M. Zhou, R. Liang, Z. Zhou, and X. Dong: Superior energy storage properties and excellent stability of novel $NaNbO_3$-based lead-free ceramics with A-site vacancy obtained via a Bi_2O_3 substitution strategy. *J. Mater. Chem. A* **6**, 17896 (2018).

29. H. Guo, H. Shimizu, and C.A. Randall: Direct evidence of an incommensurate phase in $NaNbO_3$ and its implication in $NaNbO_3$-based lead-free antiferroelectrics. *Appl. Phys. Lett.* **107**, 112904 (2015).

30. L.E. Cross and B.J. Nicholson: The optical and electrical properties of single crystals of sodium niobate. *Philos. Mag.* **46**, 453 (1955).

31. L.E. Cross: Electric double hysteresis in $(K_x Na_{1-x})NbO_3$ single crystals. *Nature* **181**,178 (1958).

32. L.E. Cross: Relaxor ferroelectrics. *Ferroelectrics* **76**, 241 (1987).

33. A.A. Bokov and Z-G. Ye: Recent progress in relaxor ferroelectrics with perovskite structure. *J. Mater. Sci.* **41**, 31 (2006).

34. X. Dai, Z. Xu, J-F. Li, and D. Viehland: Effects of lanthanum modification on rhombohedral Pb $(Zr_{1-x}Ti_x)O_3$ ceramics: Part II. Relaxor behavior versus enhanced antiferroelectric stability. *J. Mater. Res.* **11**, 626 (1996).

35. Q. Tan, J-F. Li, and D. Viehland. Ferroelectric behaviours dominated by mobile and randomly quenched impurities in modified lead zirconate titanate ceramics. *Philos. Mag. B* **76**, 59 (1997).

36. D. Viehland, X.H. Dai, J.F. Li, and Z. Xu: Effects of quenched disorder on La-modified lead zirconate titanate: long-and short-range ordered structurally incommensurate phases, and glassy polar clusters. *J. Appl. Phys.* **84**, 458 (1998).

37. J. Knudsen, D.I. Woodward, and I.M. Reaney: Domain variance and superstructure across the antiferroelectric/ferroelectric phase boundary in $Pb_{1-1.5x}La_x(Zr_{0.9}Ti_{0.1})O_3$. *J. Mater. Res.* **18**, 262 (2003).

38. Y. Feng, Z. Xu, H. Li, and X. Yao: Effect of La modifier on the electric hysteresis of lead zirconate stannate titanate compounds. *Ceram. Int.* **30**, 1393 (2004)

39. P. Mohapatra, Z. Fan, J. Cui, and X. Tan: Relaxor antiferroelectric ceramics with ultrahigh efficiency for energy storage applications. *J. Eur. Ceram. Soc.* **39**, 4735 (2019).

40. J. Chen and D. Feng: TEM study of phases and domains in $NaNbO_3$ at room temperature. *Phys. Status Solidi A* **109**, 171 (1988).

41. H. Guo, H. Shimizu, and C.A. Randall: Microstructural evolution in $NaNbO_3$-based antiferroelectrics. *J. Appl. Phys.* **118**, 174107 (2015).

42. K. Uchino and S. Nomura: Critical exponents of the dielectric constants in diffused-phase-transition crystals. *Ferroelectrics* **44**, 55 (1982).

43. N. Vittayakorn, G. Rujijanagul, X. Tan, M.A. Marquardt, and D.P. Cann: The morphotropic phase boundary and dielectric properties of the $xPb(Zr_{1/2}Ti_{1/2})O_3$-$(1-x)Pb(Ni_{1/3}Nb_{2/3})O_3$ perovskite solid solution. *J. Appl. Phys.* **96**, 5103 (2004).

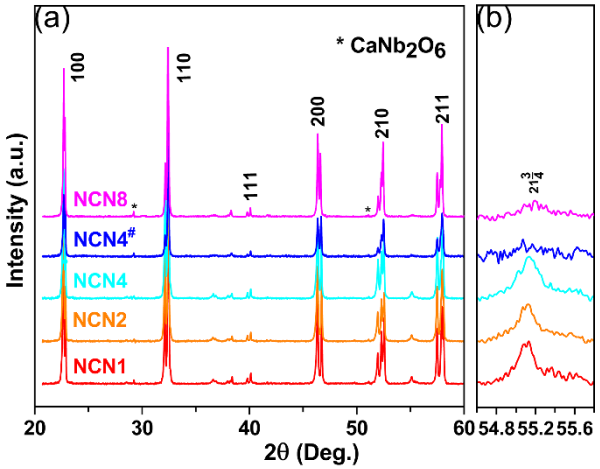

Figure 1: (a) X-ray diffraction patterns of the sintered ceramics in the 2θ range of ~20°-60°. The peaks are indexed on the basis of a pseudocubic unit cell, and the * symbol marks the peaks of the second phase $CaNb_2O_6$. (b) The highlighted $(21\frac{3}{4})_c$ superlattice peak.

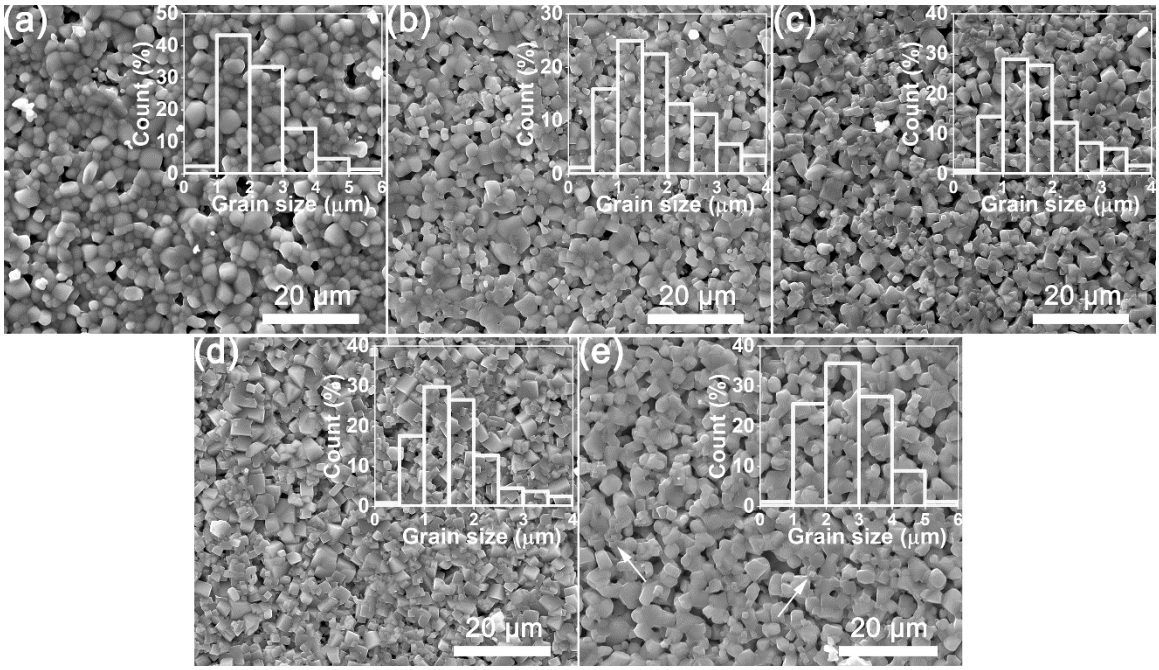

Figure 2: SEM micrographs and histograms of the grain-size distribution of as-sintered surfaces of ceramics of (a) NCN1, (b) NCN2, (c) NCN4, (d) NCN4$^{\#}$, and (e) NCN8. The two arrows in (e) mark two particles of the second phase.

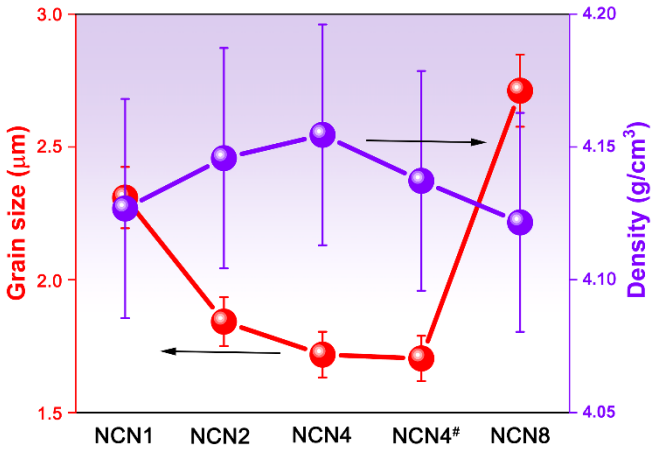

Figure 3: Average grain size and density of the studied ceramics.

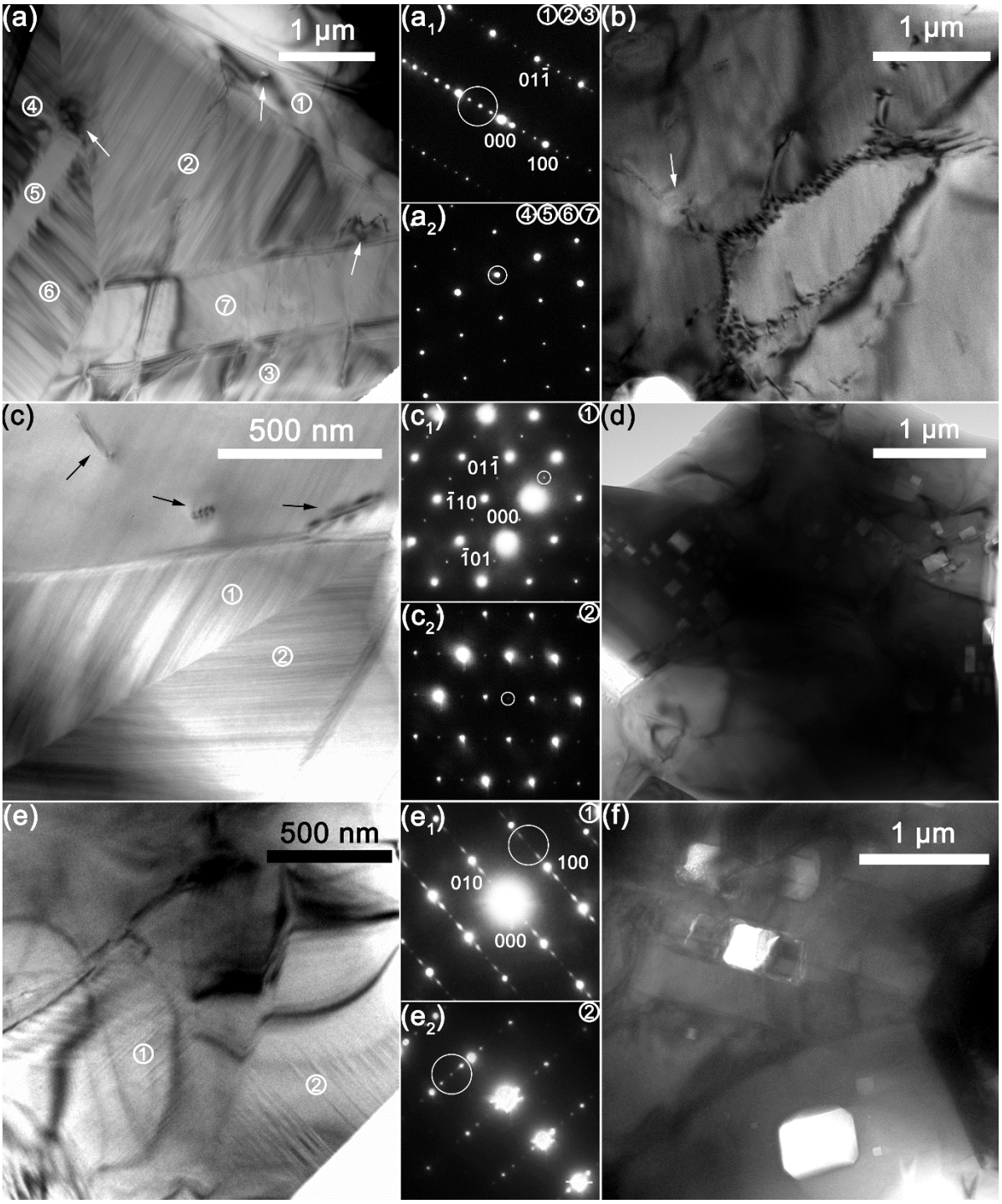

Figure 4: TEM analysis on ceramics of (a-b) NCN1, (c-d) NCN4, and (e-f) NCN8. (a_1) Selected area electron diffraction pattern (SADP) along the $[011]_c$ zone-axis from areas ①, ②, and ③ in (a). (a_2) SADP from the areas of ④, ⑤, ⑥, and ⑦ in (a). (c_1) SADP along the $[111]_c$ zone-axis from area ① in (c). (c_2) SADP from area ② in (c). (e_1) SADP along the $[001]_c$ zone-axis from area ① in (e). (e_2) SADP from area ② in (e). Bright arrows in (a) and (b) point to fine second-phase particles while dark arrows in (c) point to dislocations. Bright circles in all SADPs mark the superlattice diffraction spots.

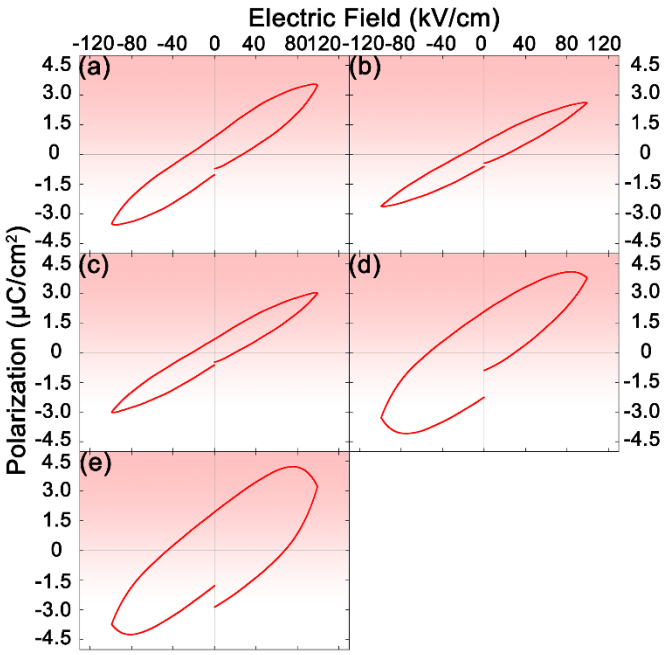

Figure 5: Electric field *vs.* polarization hysteresis loops recorded at room temperature under the peak field of 100 kV/cm. (a) NCN1, (b) NCN2, (c) NCN4, (d) NCN4$^{\#}$, and (e) NCN8.

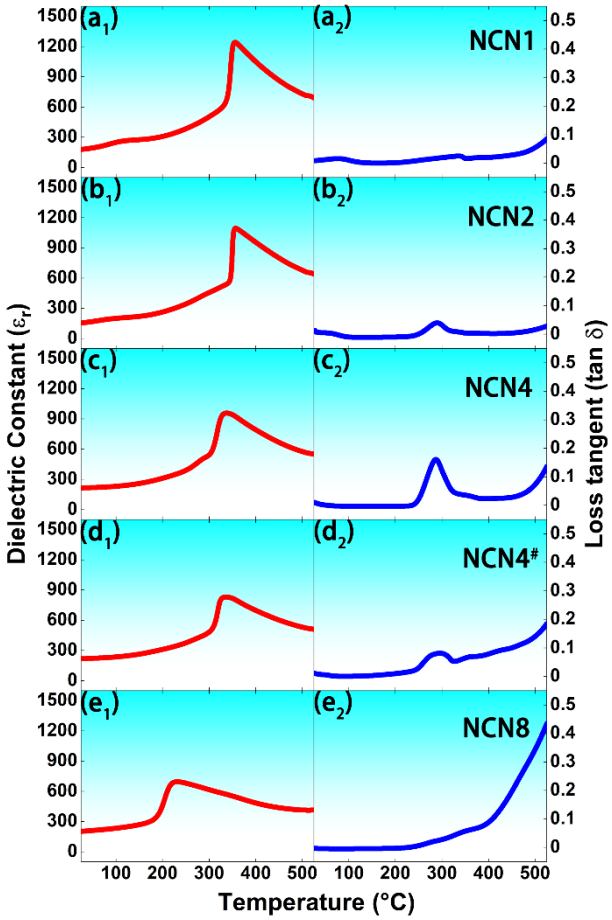

Figure 6: Dielectric constant and loss tangent of the ceramics measured at 1 MHz during heating (a_1-a_2) NCN1, (b_1-b_2) NCN2, (c_1-c_2) NCN4, (d_1-d_2) NCN4$^{\#}$, and (e_1-e_2) NCN8.

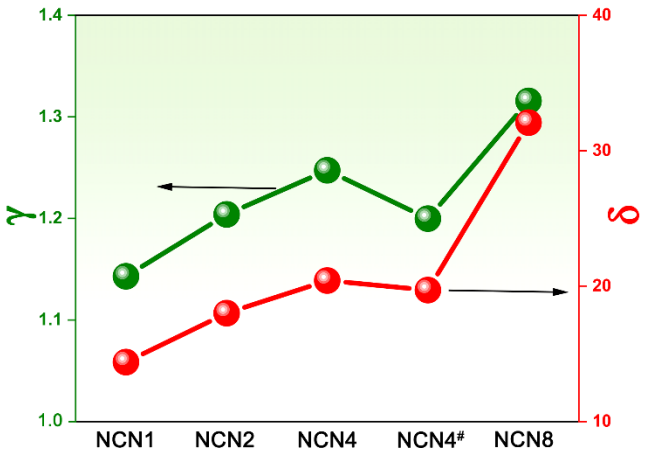

Figure 7: Relaxation parameter γ and diffuseness parameter δ obtained from fitting the 1MHz dielectric constant data.